Physica Medica 133 (2025) 104959

Contents lists available at ScienceDirect

Physica Medica

journal homepage: www.elsevier.com/locate/ejmp

Feasibility study of using fast low-dose pencil beam proton and helium radiographs for intrafractional motion management

Alexander A. Pryanichnikov [a,b,*], Jennifer J. Hardt [c,d,e], Ethan A. DeJongh [f], Lukas Martin [a,d], Don F. DeJongh [f], Oliver Jäkel [c,e,g], Niklas Wahl [c,e], Joao Seco [a,d]

[a] *Division of Biomedical Physics in Radiation Oncology, German Cancer Research Center (DKFZ), Heidelberg 69120, Germany*
[b] *Institute of Biomedical Engineering (IBT), Karlsruhe Institute of Technology (KIT), Karlsruhe, Germany*
[c] *Division of Medical Physics in Radiation Oncology, German Cancer Research Center (DKFZ), Heidelberg 69120, Germany*
[d] *Department of Physics and Astronomy, Heidelberg University, Heidelberg 69120, Germany*
[e] *Heidelberg Institute for Radiation Oncology (HIRO), Heidelberg 69120, Germany*
[f] *ProtonVDA LLC, 1700 Park St Ste 208, Naperville IL 60563, USA*
[g] *Heidelberg Ion-Beam Therapy Centre (HIT), Department of Radiation Oncology Heidelberg University Hospital, Heidelberg 69120, Germany*

ARTICLE INFO

Keywords:
Proton therapy
Ion beam therapy
Proton imaging
Helium imaging
Motion management
Adaptive radiation therapy

ABSTRACT

Purpose: This study aims to evaluate the feasibility of using fast, low-dose proton (pRad) and helium (HeRad) radiography for intrafractional motion management. This approach uses pencil ion beam delivery systems, modern particle imaging detectors and fast image reconstruction.
Methods: A plastic respiratory phantom underwent four-dimensional computed tomography (4DCT) using a commercial X-ray scanner, experimental pRad with a continuous proton beam from a clinical serial cyclotron, and experimental pRad and HeRad with pulsed proton and helium beams from a synchrotron-based ion therapy facility. Open-source patient 4DCT data were used in a Monte Carlo simulation study to evaluate pRad and HeRad in a realistic patient geometry. Treatment plans involving mixed carbon-helium beams were calculated using matRad and simulated in TOPAS.
Results: The experimental pRad achieved a temporal resolution of 8 fps for the cyclotron-based facility, while both pRad and HeRad achieved 2 fps for the synchrotron-based facility within a 10 cm × 10 cm region of interest. pRad reconstructed the respiratory phantom motion pattern with a dose of less than 2 μGy per image. In simulations of mixed carbon-helium beams, HeRad, both integral and single *iso*-energy, detected water equivalent thickness differences with sub-millimeter accuracy across different phases of the patient's 4DCT data.
Conclusion: This study demonstrates that low-dose small-field proton and helium radiography, utilizing pencil beam scanning, can effectively monitor intrafractional anatomical displacements with millimeter-level spatial accuracy and sub-second temporal resolution. Current particle imaging and beam delivery technologies have the potential to enable real-time patient monitoring in promising mixed ion beam therapy.

1. Introduction

Particle therapy using scanning beams has become a well-established approach for the treatment of static tumors, offering more conformal dose distributions compared to conventional photon therapy [1]. However, the high degree of conformality associated with this approach leads to significant geometric and dosimetric uncertainties when intrafractional motion is taken into account [2–5]. A randomized trial [6] demonstrated that proton therapy for non-small cell lung cancer (NSCLC) did not significantly improve lung outcomes or reduce toxicity compared to photon therapy, with its potential benefits being diminished by intrafractional motion and range uncertainties [7]. Respiratory motion is a major source of intrafractional motion and can significantly affect tumors located in the thorax [8] and abdomen [9], it is critical to have a qualitative and quantitative analysis of this motion.

The American Association of Physicists in Medicine (AAPM) TG-76 report [10] quantified lung tumor motion and found displacements of 18.2 mm in the superior-inferior dimension, 9.5 mm in the anterior-posterior dimension, and 10.5 mm in the left–right dimension. A more recent study [11] reported the amplitude of gross tumor volume (GTV)

---

* Corresponding author at: Division of Biomedical Physics in Radiation Oncology, German Cancer Research Center (DKFZ), 69120, Heidelberg, Germany.
E-mail address: alexander.pryanichnikov@dkfz-heidelberg.de (A.A. Pryanichnikov).

https://doi.org/10.1016/j.ejmp.2025.104959
Received 21 December 2023; Received in revised form 18 February 2025; Accepted 22 March 2025

motion in common NSCLC cases to be 5.0 ± 2.8 mm and recommended the use of 4D computed tomography (4DCT) [12] for treatment adaptation within proton therapy. To address the challenges of tumor motion during particle therapy, several dose delivery techniques have been developed [13,14]. These include internal target volumes (ITVs) [15], repainting or rescanning [16], respiratory gating [17], tumor tracking [3], 4D and robust optimization [18,19].

Particle imaging can be used as an alternative or complement to these methods to provide anatomical information while not being significantly affected by range uncertainties [20]. One potential solution involves fast change of ion beam energies to switch between imaging (shoot-through) and treatment (stopping the beam within the target volume). Another approach is to use two particles with a constant mass-to-charge ratio (e.g. $^{12}C^{6+}$ and $^{4}He^{2+}$) for simultaneous imaging and treatment. The concept of using mixed carbon and helium beams, with helium as the range probe, was originally proposed for online monitoring by two groups [21,22]. Recently, Voltz et al. [23] investigated the possibility of implementing this approach at the synchrotron-based facility. The scanning area would be aligned with the tumor volume, and the scanning time for a single slice would be negligible compared to the time of organ motion during the respiratory cycle.

Several studies have highlighted the potential of proton (pRad) and helium (HeRad) radiography for daily patient positioning [24,25]. However, these studies were focused on the imaging of the static locations, while the protocols of moving objects ion radiography with therapeutic scanning particle beams are required. One study showed the scenario of using pRad for adapting proton therapy in the treatment of thoracic tumors [26], but with proton beam intensities close to therapeutic levels. This study aims to fill the gap by developing strategies and evaluating the technical feasibility of low-dose proton (for fast multi-energy extraction) and helium (for mixed-beam approaches) radiography of moving objects fast enough to quantify respiratory motion, with a focus on its potential implementation for managing intrafractional motion in particle therapy with scanning beams.

2. Materials and methods

This study consists of both experimental and simulation components. The experimental component involved proton and helium radiography of a respiratory phantom performed at two sites: the Northwestern Medicine Chicago Proton Center (NMCPC) and the Heidelberg Ion-Beam Therapy Center (HIT). The simulation component focused on evaluating the dose load of proton and helium radiography and simulating patient-specific scenarios using a mixed carbon-helium ion beam approach.

2.1. Respiratory phantom

The phantom used was a koala toy model GRT59 (Fisher-Price, East Aurora, NY, USA) with moving parts designed to simulate human breathing. Inside the phantom is a plastic block measuring 22 cm × 7 cm × 3.5 cm, encased in a textile shell. This block contains a microcontroller, batteries, an electromechanical drive, and a small plastic platform responsible for the motion (Fig. 1A). The motion of the phantom follows a simple sine function:

$$f(t) = f_0 + A \times \sin\left(\frac{2\pi}{T} \times t + p_0\right) \tag{1}$$

where f_0 – displacement at t = 0, A – amplitude, T – period and p_0 –phase at t = 0.

The amplitude was measured using an inextensible thread and a Dahle 10,684 ruler, and the period was measured using a Samsung S21 stopwatch application.

2.2. Imaging equipment

X-ray computed tomography (CT) scans of the respiratory phantom were acquired at the DKFZ using the SOMATOM Definition Flash (Siemens Healthcare GmbH, Erlangen, Germany) with a voltage of 120 kV. Data were collected for 10 different phases of the respiratory motion in stop-and-shoot mode. Phase sorting was used to correlate the phases of the phantom's motion, with shots taken every 0.3 ± 0.1 s according to stopwatch readings. A CT slice of the moving region of interest (ROI) within the phantom is shown in Fig. 1B, where image reconstruction artifacts are visible due to the metal components of the phantom, causing saturation in certain regions.

Proton and helium radiography data were obtained using a prototype of the ProtonVDA proton imaging system [27]. This system operates in list-mode configuration, where tracking detectors record the trajectories of individual protons, and a range detector measures the water equivalent path lengths (WEPL) of each proton. These measurements allow for the reconstruction of a 2D, or 3D map of relative stopping power (RSP) values for the region of interest (ROI) and the entire phantom [28]. The system has a maximum scan field size of 40 cm × 40 cm and a data acquisition rate of 3 MHz [29]. For helium data acquisition, the system's photomultiplier voltage was lowered. Simple back-projection along the MLP was used for image reconstruction for pRad and HeRad, and the water equivalent thickness (WET) uncertainty per pixel was estimated using the following equation [30]:

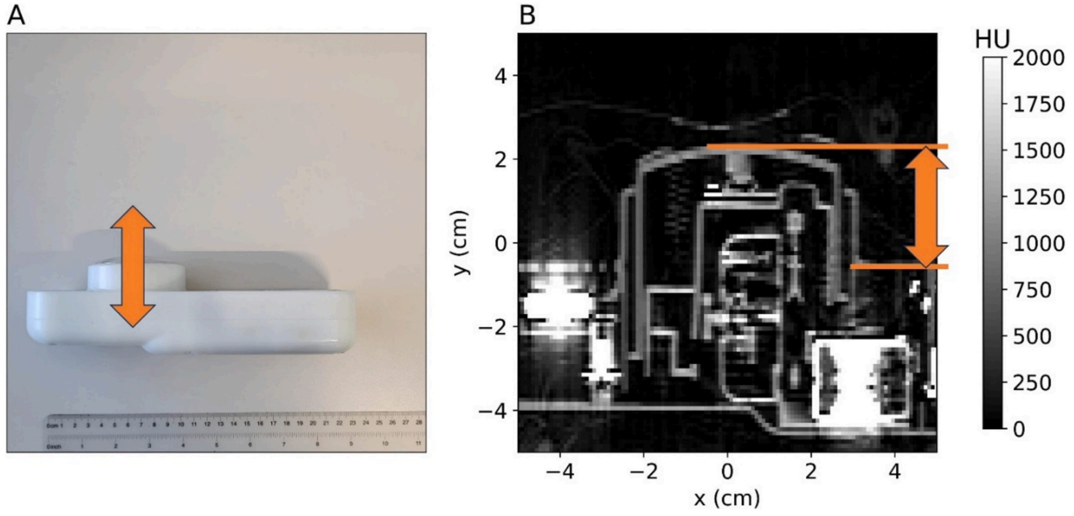

Fig. 1. A photograph of the internal part of the phantom (A) and a sagittal view of the phantom obtained using clinical CT (B).

$$\frac{3\,mm}{\sqrt{N_p}} \tag{2}$$

where N_p is the number of particles intersecting that pixel.

After image reconstruction, all experimental imaging modalities, XCT, pRad and HeRad, were correlated in terms of motion phases.

2.3. Experimental proton and helium imaging setup and beam delivery

The first experimental pRad data acquisition was conducted on the respiratory phantom at the NMCPC facility in December 2022. This facility employs an IBA C230 cyclotron (IBA, Louvain-La-Neuve, Belgium) that generates continuous proton beams. The proton imaging system was positioned on a fixed horizontal beamline equipped with pencil beam scanning (PBS) technology. The phantom was fixed inside the proton imaging system using standard plastic tape (approximately 300 µm thick), with the central part of the movable element aligned with the particle imaging detector's center. The motion pattern was reconstructed from pRad images by tracking the distance between the stationary and moving parts of the phantom as indicated in Fig. 1B.

The phantom was irradiated in the spot scanning mode. The single energy of the 120 MeV beam was used with a beam profile width at the isocenter of $\sigma_x \approx \sigma_y \approx 7.0$ mm and a divergence of approximately 2.9 mm^{-1}. A 10 cm × 10 cm field with a spot spacing of 0.5 cm (21 × 21 spots) was scanned from top right to bottom left, requiring 130 ms and utilizing approximately 2×10^5 protons (400–500 protons per spot). Each spot required approximately 0.1 ms of delivery time, after which the scanning magnet was switched to another point required an additional 0.1–0.3 ms of time, depending on spot position. A total of 60 scans were performed on the continuously moving phantom without any stops between the scans.

The second experimental pRad and HeRad data acquisition was conducted at HIT in July-August 2024 using the same respiratory phantom and proton imaging detector. HIT [31,32], a synchrotron-based facility, operates with multiple particle species, including protons, helium, and carbon ions in a pulsed beam mode. Following the NMCPC protocol, particle imaging was performed using a 121.95 MeV proton beam $\sigma_x \approx \sigma_y \approx 5.6$ mm at the isocenter. The same 21 × 21 spot pattern was used from top right to bottom left, requiring 560 ms per scan and using approximately 5×10^5 protons (1000–1200 protons per spot) over 10 scans. For HeRad, an 80.64 MeV/u helium beam with $\sigma_x \approx \sigma_y \approx$ 4.9 mm was used, requiring 450 ms per scan and utilizing approximately 0.5——2×10^5 helium ions (150–600 ions per spot). Each spot required 1.2–1.3 ms for the pRad case and about 1.0 ms for the HeRad case. The time to move the beam between stops was less than 0.1 ms. The limitation of 10 scans was only due to the pulsed nature of the synchrotron, after 5 s of extraction it was necessary to start the next cycle with a pause of several seconds needed to inject and accelerate a new beam. The phantom position was shifted by 2 cm in the vertical direction compared to the previous measurements.

2.4. Monte Carlo simulations

Simulated images were generated using TOPAS version 3.9 [33], an extension of GEANT4 designed for particle therapy applications [34]. The simulations included a comprehensive set of physical processes for proton and helium ion interactions in the intermediate energy range, covering both electromagnetic and hadronic processes [35]. Following Volz et al. [23], several physics lists were employed, including G4HadronElasticPhysics, G4ExtraPhysics, LXeEMPhysics, LXeMuonPhysics, G4StoppingPhysics, G4DecayPhysics, and G4QMDReaction, with the helium region modeled using G4BinaryLightIonReaction and the Tripathi cross section data [36] modified by [37]. The standard Hounsfield units (HU) transformation built into TOPAS was used for CT data [38].

The imaging detector model consisted of tracking detectors segmented into stacks of 1 mm scintillating fibers, positioned 30 cm apart around the respiratory phantom. The scintillating fibers were arranged in two layers offset by 0.5 mm, allowing for proton localization to 0.5 mm in each direction per plane [27]. WEPL resolution was simulated by modelling detector response across various positions and residual ranges. Simulated WEPL was reconstructed using the same method as for real data [27].

The time feature of the TOPAS framework was used to simulate the dynamic nature of the experiments. All phases of the motion-binned 4DCT data of the phantom were used to generate a sequence of the geometry instances by interpolating the data on the moving part of the phantom according to formula (1). These geometries were updated in the framework every 0.33 ms and used to create the simulated pRad images. Following the first experimental protocol, the simulation was run from the randomly selected geometry instance and was performed for 60 beam scan patterns (10 cm × 10 cm field, 500 protons per spot). Each spot was irradiated for 0.1 ms, followed by a 0.2 ms pause, resulting in a total scan duration of 132.3 ms, which corresponds to the experimental measurement performed at NMCPC.

2.5. Simulated patient case

The 4DCT data for proton and helium imaging simulations were obtained from the open Cancer Imaging Archive [39]. Data from NSCLC patients were acquired using a 16-slice helical CT scanner (Brilliance Big Bore, Philips Medical Systems) with Real-time Position Management (Varian Medical Systems). A voltage of 120 kV was used, and respiration-correlated CTs with 10 breathing phases were obtained (0 % to 90 %, phase-based binning), with the 0 % phase corresponding to the end of inhalation. Data from patient #102 were used for further illustrations.

pRads and HeRads of the patient 4DCT data (40 cm × 40 cm, the maximum size allowed by the detector) were simulated to estimate the dose load in both cases. The scintillating fibers were positioned 60 cm apart from the central point of the 4DCT DICOM patient data. Images were acquired using 2000 ions per spot, spaced at 1 cm intervals, with a beam profile $\sigma_x \approx \sigma_y \approx 7.0$ mm. Two projections (anteroposterior and lateral) were simulated using monoenergetic beams of 220 MeV/u and 300 MeV/u.

A framework was developed [40] in the open-source irradiation planning software matRad [41,42] to explore the concept of using mixed carbon and helium beams for ion beam therapy. A treatment plan for a lung cancer patient was devised using this mixed beam approach. Initially, the carbon ion dose was optimized on the first phase of the 4DCT, followed by the calculation of the corresponding mixed-in helium ion dose. A previous study [23] showed that adding 10 % helium ions generates a detectable helium signal above the carbon fragment background. The treatment planning involved the pencil-beam algorithm in matRad, and dose recalculation was performed using a research extension of matRad that interfaces with TOPAS, allowing evaluation of the detection response during treatment and reconstruction of radiographs from primary helium ions passing through the patient.

The treatment plan involved two treatment angles (45°, 90°) and used 3×10^4 spots with 103 different energy levels. If executed, the plan would involve 3.7×10^9 carbon particles. Additionally, a reduced treatment plan using a single energy per angle (1.1×10^8 carbon particles) was simulated. For the patient case 10^7 (full plan), and 10^5 (reduced plan) histories were simulated, representing 3 % (full plan) and 1 % (full plan) of the total helium particles required. The simulation of carbon and helium was sequential, neglecting carbon fragment contributions to the detection system. Radiographs were reconstructed using WEPL estimates from residual energy of the helium ions.

3. Results

3.1. Experimental phantom pRad for cyclotron-based facility

60 pRads obtained at NMCPC (as described in section Experimental proton images) were reconstructed. Fig. 2 shows the pRads for the maximum negative displacement of the moving part (0 %), the default position (40 %), and the maximum positive displacement (90 %). These images were used to estimate the temporal resolution of the setup and to reconstruct the motion pattern of the phantom as described in section Respiratory phantom.

Fig. 3A illustrates the single pixel WET sensitivity of the experimental setup. The pixel with coordinates (0 cm, 0 cm) was chosen to illustrate the change in WET over time. The maximum difference of 2.5 cm WET was recorded between the phases of the phantom motion. The averaged WET uncertainty was 0.07 cm. The maximum difference between the left and right edges of the moving part of the phantom in the same image was 1 pixel.

To reconstruct the motion pattern, the measured distances (see section Respiratory phantom) were fitted with a sine function (1): $f_0 = 1.198 \pm 0.010\,\text{cm}$, $A = 1.130 \pm 0.014\,\text{cm}$, $\frac{2\pi}{T} = 1.913 \pm 0.006\,\frac{Rad}{s}$, $p_0 = 0.34 \pm 0.03\,\text{Rad}$ as shown in Fig. 3B. The amplitude and the period $T = 3.28 \pm 0.01\,\text{s}$ are within error with the values set and measured by conventional tools: $A_{meas} = 1.10 \pm 0.05\,\text{cm}$ and a period $T_{meas} = 3.3 \pm 0.1\,\text{s}$.

3.2. Experimental phantom pRad and HeRad for synchrotron-based facility

Additional 10 pRads and 10 HeRads obtained at HIT were reconstructed as demonstrated in Fig. 4. The amplitude and period were calculated as above for protons $A_{pRad,HIT} = 1.24 \pm 0.10\,\text{cm}$ and a period $T_{pRad,HIT} = 3.4 \pm 0.1\,\text{s}$ and for helium ions $A_{HeRad,HIT} = 1.28 \pm 0.14\,\text{cm}$ and a period $T_{HeRad,HIT} = 3.5 \pm 0.2\,\text{s}$. The currently obtained experimental helium images suffer from a high noise level which is the result of two factors: unstable beam extraction for the low intensity beam (150–600 ions per spot as detailed in the Materials and Methods section) and lack of proper required adjustment of the particle imaging detector parameters since the detector is optimized for proton beams.

3.3. Simulated phantom CT-based pRad

The simulated pRads of the respiratory phantom were compared to the acquired radiographs, benchmarking the experimental measurements against a Monte Carlo simulation that incorporated the interpolated data from the X-ray 4DCT to better mimic the experimental conditions (Fig. 5).

The dark areas in the lower right corner of the simulated images are caused by unrealistically high HU values in the CT data due to the presence of metal in the moving part of the phantom. Due to incorrect material conversion, the protons cannot pass through these areas in the simulation, making it impossible to reconstruct their paths. Similarly, the bright region in the lower left corner contains artifacts caused by incorrect material conversion in the original data. These two regions are the only areas that appear saturated. Within these areas, the simulated WET values differ from the experimental pRad image (Fig. 4C) by more than 10 % in the CT-based comparison, with a localized WET difference of 1 cm near the metal inserts (Fig. 4C). The validation of the experimental versus simulated pRads was performed for 10 motion phases, ranging from 0 % to 90 % of the motion amplitude. Excluding the artifact-affected regions, a WET difference greater than 2 mm between the simulated and experimental images was observed in less than 7 % of the image area, primarily due to noise in the experimental image. No correlation between motion phase and the error pattern was detected.

The breathing curve parameters of the phantom were measured from 60 simulated pRads, following the same methodology as for the experimental data, the amplitude $A_{sim} = 1.12 \pm 0.02\,\text{cm}$ and a period $T_{sim} = 3.29 \pm 0.01\,\text{s}$ were calculated.

Monte Carlo simulation data were used also to estimate the dose to the irradiated area of the phantom. The averaged dose for a series of 60 simulated pRads was 1.83 ± 0.05 μGy.

3.4. Simulated patient CT-based pRad and HeRad

Since this study aimed to evaluate the feasibility of fast, low-dose particle radiography for motion management and verification of anatomical changes, the physical model (see Monte Carlo simulations section) was used to generate pRad and HeRad images (using HIT beam parameters and particle imaging detector geometry) from patient CT data to estimate patient dose across different particle radiography modes.

The resulting dose for full-scale pRads were 12.6 ± 1.1 μGy for AP and 13.8 ± 0.8 μGy for the lateral projections, respectively. These values were averaged for the irradiated areas and each phase of the 4DCT. Analogous HeRads were modeled. The resulting doses were 18.0 ± 1.3 μGy and 19.9 ± 1.4 μGy for two projections (AP and lateral). The WET uncertainty averaged over the image was 0.65 mm for both pRad and HeRad. The average physical dose difference for protons and helium ions for the simulated images was up to 44 %. Dose parameters given here and above represent the physical dose in Gy, without consideration of radiation weighting factors for protons and helium ions.

After simulation of the full-scale images, mixed beam HeRads of irradiated volume were simulated for two angles. To explore the application of the mixed carbon-helium beam technique for managing motion

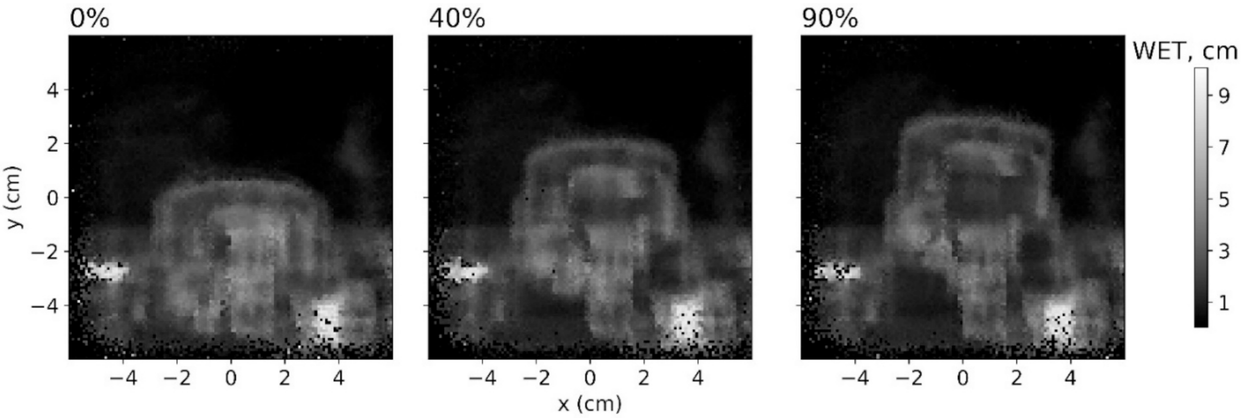

Fig. 2. Reconstructed pRads at NMCPC for three phases of the moving phantom (0%, 40% and 90%).

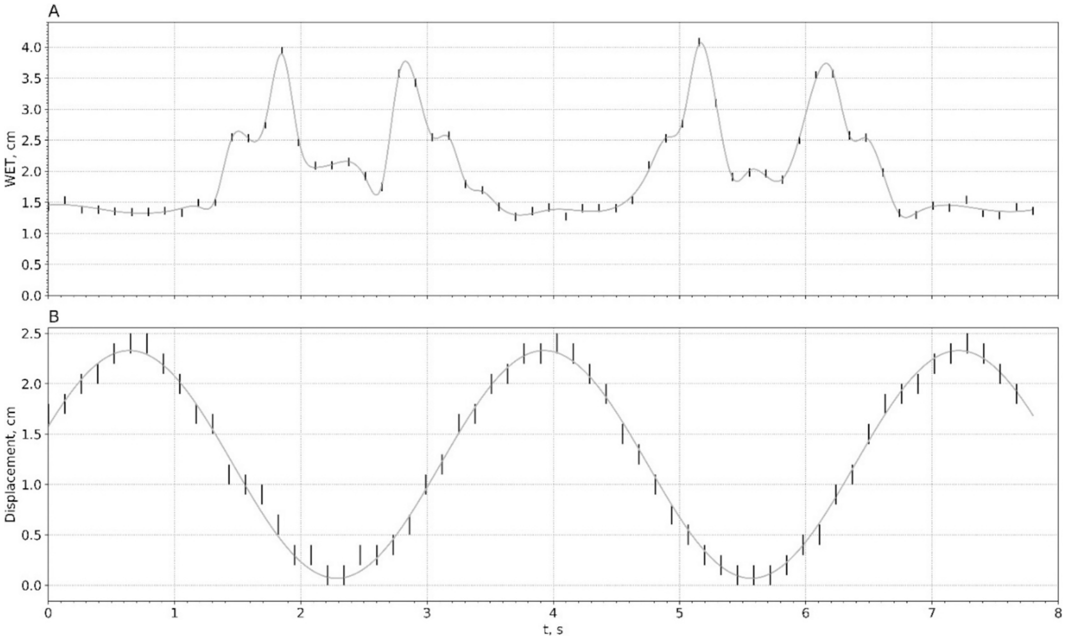

Fig. 3. pRads parameters of scanned moving phantom at the NMCPC: (A) WET of a central pixel (0 cm, 0 cm) over time; (B) displacement of the moving phantom part over time and the sine fit.

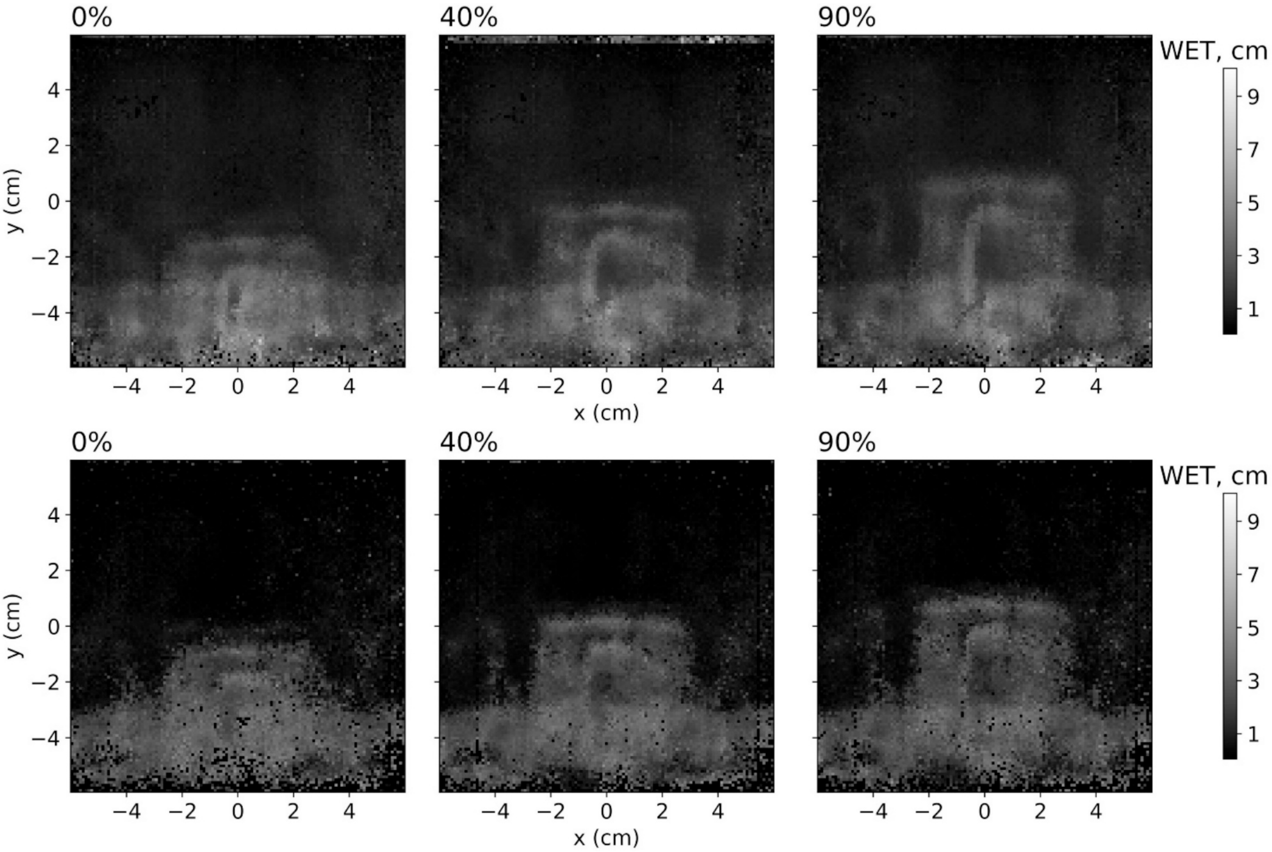

Fig. 4. Reconstructed pRads (top row) and HeRad (bottom row) at HIT for three phases of the moving phantom.

during treatment, the simulated HeRads were evaluated. The results for phase 0 % of the lung patient are shown in Fig. 6A and 6C, which show a 2D reconstruction of the treated anatomy. These images have a total number of pixels of 300 × 300 with a pixel size of 1 mm × 1 mm. After reconstructing the images, they were converted into two-dimensional matrices with values from 0 to 255, then by manually selecting the threshold, they were converted into matrices of the same dimensionality but with values (0,1) and contoured as shown in Fig. 6C and D, respectively.

The contour displacement was recorded for each of the phases, and

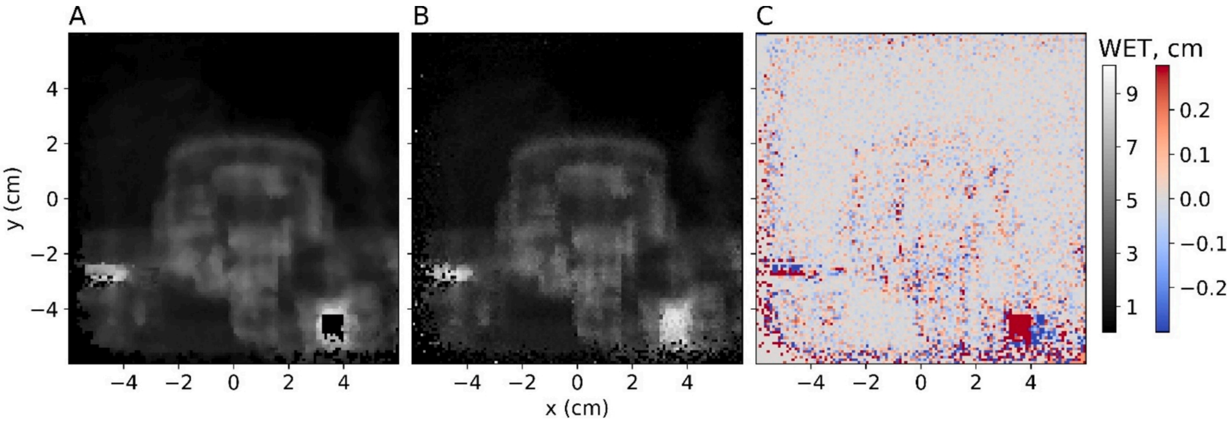

Fig. 5. Comparison of simulated and experimental pRad images obtained at the NMCPC: (A) Simulated pRad based on 4DCT phantom data with interpolation between phases; (B) Experimental pRad of the corresponding phase of the motion; (C) Difference in absolute value of WET between simulated CT-based pRad and experimental pRad.

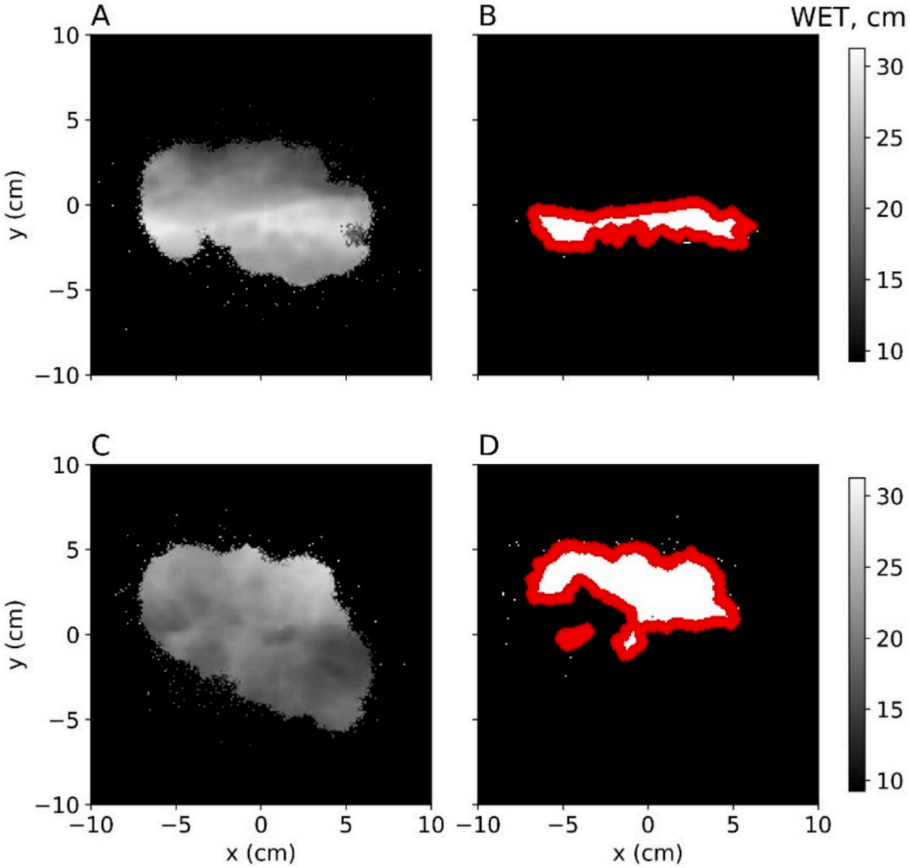

Fig. 6. Simulated HeRads for two fields of the mixed carbon-helium treatment plan of the phase 0% (day 1) of patient #102: (A) PTV HeRad at 45° treatment angle; (B) PTV HeRad (45°) contour with a threshold of 190 out of 255; (C) PTV HeRad at 90° treatment angle; (D) PTV HeRad (90°) contour with a threshold of 150 out of 255, where the red line corresponds to the contour boundary.

then the data were fitted with a slightly modified sine function (1): $f(t) = f_0 + A \times \sin(\frac{2\pi}{10} \times t + p_0)$. Since the exact time for each phase was unknown from the original data, each phase was used as a separate time quantum, equal to 0 through 9. In this way, the coefficient responsible for the period of the sine function can be fixed at $\frac{2\pi}{10}$. Based on these data, the amplitude displacements of the selected contours were reconstructed. The results for integral HeRads are shown in Table 1.

The HeRads in Fig. 6 were reconstructed using data from all energies in the treatment plan. However, for any synchrotron-based facility, there is a delay between the extraction of beams of different energies, on the order of 0.1 to 10 s. Therefore, the next logical step was to extrapolate the results obtained to the individual energies of the mixed beam treatment plan. Here, the irradiated volume of a single energy HeRad is smaller because not every region of the tumor is scanned with every energy.

Single energy (232.2 Mev/u and 223.56 Mev/u) HeRads were simulated according to the treatment plan of the same irradiation volume. Fig. 7A, D, B, E show single energy HaRad for two fields and phase

Table 1
The sine fit amplitude coefficients for the integral and single energy HeRads in mixed beam mode.

Type of HeRad	Direction	*A, cm*
All energies, 1st field	X	1.97 ± 0.15
All energies, 1st field	Y	1.09 ± 0.17
All energies, 2nd field	X	−3.8 ± 0.2
All energies, 2nd field	Y	1.09 ± 0.09
Single energy, 1st field	X	2.01 ± 0.13
Single energy, 1st field	Y	0.94 ± 0.09
Single energy, 2nd field	X	−3.3 ± 0.2
Single energy, 2nd field	Y	1.08 ± 0.09

0 % and 40 %, respectively. Fig. 7C and F show the difference in patient anatomy positioning for these two phases. These images were also converted and contoured as above, the contour displacements were also fitted with a sine function with fixed period, the coefficients of which are given in Table 1 in the last 4 rows. The averaged over the image WET uncertainties were 0.34 mm and 0.24 mm for the 1st and the 2nd fields, respectively.

As can be seen from Table 1, the displacement amplitude along Y for all four cases coincides within errors. The values of the contour displacement of the first field by X, also coincide in the error bars for integral (AI) and single energy (SE) images: $A_{\mathrm{AI,\,x,\,field\,1}} = 1.97 \pm 0.15\,\mathrm{mm}$ and $A_{\mathrm{SE,\,x,\,field\,1}} = 2.01 \pm 0.1\,\mathrm{mm}$. For the second contour displacements, the obtained values do not coincide by 13 %, which is

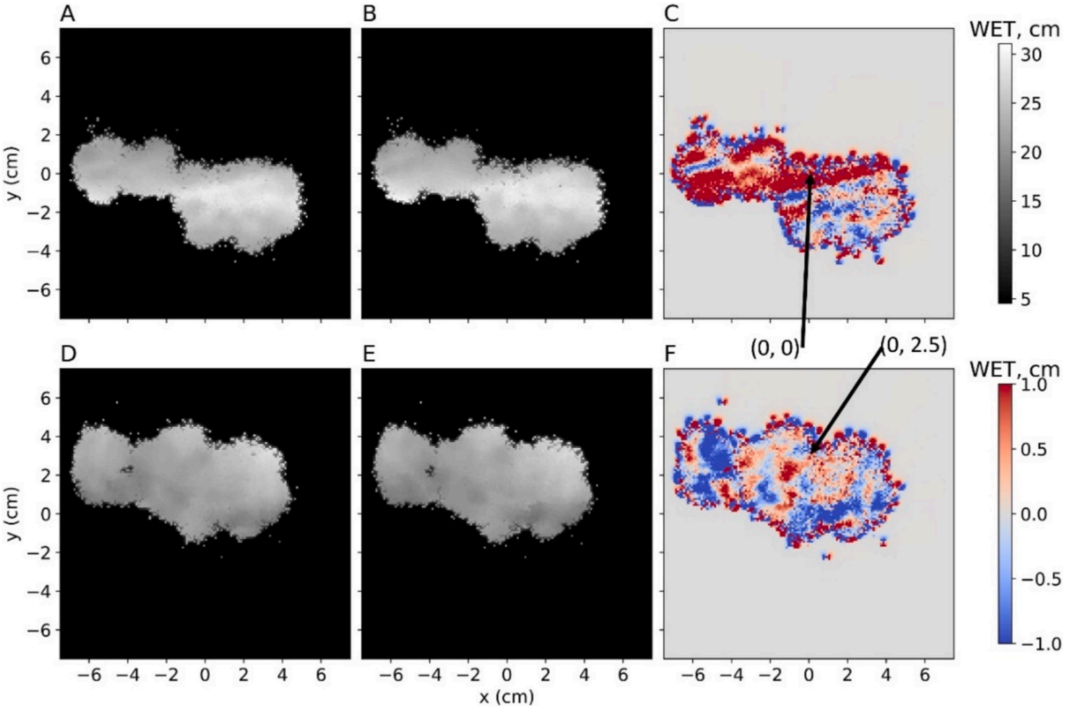

Fig. 7. The following HeRads were obtained: HeRad (A): 1st field, phase 0%; HeRad (B): 1st field, phase 40%; HeRad (D): 2nd field, phase 0%; HeRad (E): 2nd field, phase 40% of 4DCT. Images (C) and (F) demonstrate the difference in WET when executing a treatment plan optimized for the 0% phase to the 40% phase of the 4DCT data. Black arrows indicate pixels with coordinates (0, 0) and (0, 2.5) cm.

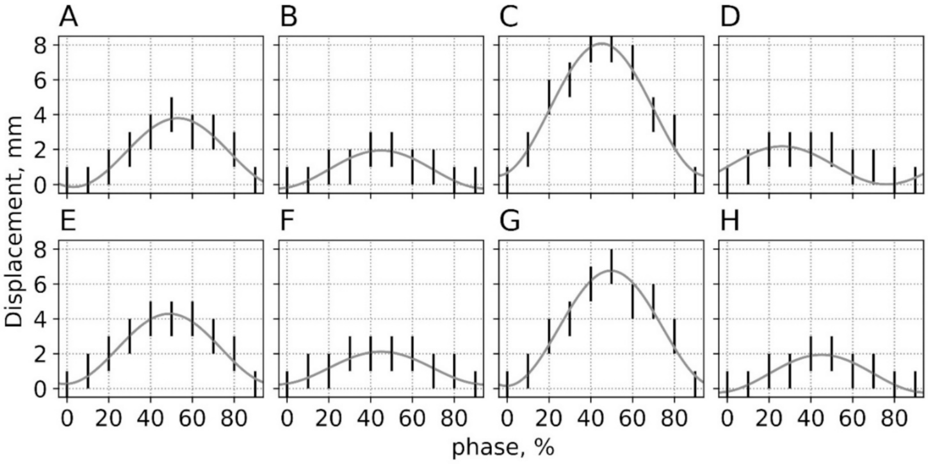

Fig. 8. Sine fit of contour displacements: (A) Integral HeRad, 1st field, X direction; (B) Integral HeRad, 1st field, Y direction; (C) Integral HeRad, 2nd field, X direction; (D) Integral HeRad, 2nd field, Y direction; (E) Single energy HeRad, 1st field, X direction; (F) Single energy HeRad, 1st field, Y direction; (G) Single energy HeRad, 2nd field, X direction; (H) Single energy HeRad, 2nd field, Y direction.

0.5 mm in absolute values: $A_{\mathrm{AI,\,x,\,field\,2}} = 3.8 \pm 0.2$ mm and $A_{\mathrm{SE,\,x,\,field\,2}} = 3.3 \pm 0.2$ mm respectively. All fitting functions for the motion period (10 phases from 0 % to 90 %) are shown in Fig. 8.

The total physical dose per mixed beam treatment plan was 1.8 Gy. The dose impact of the helium beam was approximately 2.4 % (1.76 Gy for the carbon beam and 0.04 Gy for the helium beam, respectively). For integral HeRad, the dose mixed-in helium beam was 25.3 mGy and 17.5 mGy for both projections (1.05 Gy and 0.7 Gy for carbon beam). For single energy HeRad, the helium beam dose was 0.7 mGy and 0.4 mGy for both projections (34.3 mGy and 17.6 mGy for carbon beam). The ratio of the physical dose of the helium beam to the total dose was in the range of 2.1 % to 2.5 % for all scenarios.

4. Discussion

Particle therapy encounters a distinct challenge in dealing with intrafractional motion, which introduces increased uncertainty in range and dose due to interactions caused by the patient's anatomical motion and the delivery sequence of the scanning beam. This paper considers and illustrates low-dose proton and helium radiography as a potential means of directly monitoring and controlling anatomical displacement and motion. This can be achieved by pre-adapting executable plans for protons or even real-time monitoring using a combination of helium and carbon beams. The results of this study demonstrated the potential of using the combination ProtonVDA detector and IBA C230 or HIT beam delivery systems to check for intrafractional changes for relatively small field of view.

In this work, we have shown that for selected combination of the equipment and small scanning regions, it is possible to achieve a temporal resolution of 0.13–0.56 s, which is comparable with modern commercial optical systems for surface-guidance (0.07 s – 0.6 s) [43]. This resolution is affected by the selected scan pattern and the detector response time. Since the detector can measure the parameters (positions in both fiber detector and residual energy of primary ion) of particle events in the order of 10^{-7} s, the limiting factor was the scan pattern, determined by the beam extraction rate and the speed of the scanning magnets, where each spot required about 10^{-4} s.

The MLP binning method was used to reconstruct pRads and HeRads. We also have the option of performing an iterative 3D reconstruction using the curved trajectories of the protons and helium ions as determined by MLP and then collapsing the result into a 2D image [30]. This approach produces slightly sharper images but also increases noise and requires much more computation [44]. However, for monitoring WET changes during treatment, the MLP binning algorithm is more appropriate and can be performed within a few seconds.

For the implementation of real-time monitoring, we consider two strategies based on the mixed-beam approach, namely single-energy analysis (SEA) and single-spot range probe (SSRP). Both strategies will incorporate an external surrogate respiratory monitor, such as surface-guided (SG) systems, which reduces the amount of imaging required [45]. In both scenarios, the SG system will provide the trigger to start the irradiation, since only after starting the plan execution it is possible to get the range information from the imaging (helium) beam. The respiratory signal (Fig. 9a) is obtained by the SG system, which generates triggers (Fig. 9b) for the start and end of a predetermined phase. The range-guided (RG) system provides triggers (Fig. 9c) in the case of failure of single or multiple averaged WET fast checks. The accelerator control system provides a signal (Fig. 9d) when the beam is accelerated up to the needed energy and is ready for extraction. A microcontroller (μCU) compares signals (Fig. 9b-d) and generates a resulting signal (Fig. 9e) or gates for beam delivery. Based on the execution status of the irradiation plan, feedback on beam delivery is sent to the accelerator control system.

The SEA (which can be implemented first) involves an *iso*-energy layer-by-layer analysis of the executed plans. We designed this solution for synchrotrons, where the plans are executed energy by energy, with a transition time between each *iso*-energy layer of several seconds. This time delay between energies allows an accurate analysis of the *iso*-energy HeRad in the ROI by comparing the planned data with the executed results. If a significant discrepancy is detected, the irradiation is stopped to investigate the cause. In cases where the discrepancy is not critical, the analysis data is used to adjust the treatment plan between fractions. The combination of information obtained in this way gives an idea of the real motion pattern and can be more accurately correlated with an external SG, thus opening the possibility of adapting the "treatment plan of the day" just before the treatment is scheduled to be delivered, i.e. adapt subsequent fractions according to already completed ones.

The second strategy, SSRP, is based on a fast analysis of the average WET values for each spot or small group of spots. The corresponding table of values is loaded into the RG system and a threshold value is selected. If the WET value exceeds this threshold, an interlock is triggered that stops irradiation until the end of the next respiratory pause indicated by the SG system. As can be seen in Fig. 10, the WET difference for a single pixel can be a few centimeters, while the average WET does not change significantly. According to the clinical guidelines, the threshold value can be chosen as a few mm, which allows a small number of particles touching each pixel. The general workflow of the SSRP is as follows: the SG system detects patient motion caused by respiration and sends the generated triggers to the microcontroller. Beam readiness data from the accelerator control systems is also sent to the microcontroller. In addition, the RG system can send a signal to stop irradiation, as described above. The beam delivery system keeps track of the number of particles extracted and, if necessary, requests an additional cycle to compensate for underdosing through feedback mechanisms.

The concept of *iso*-energy layer analysis now seems to be ready for

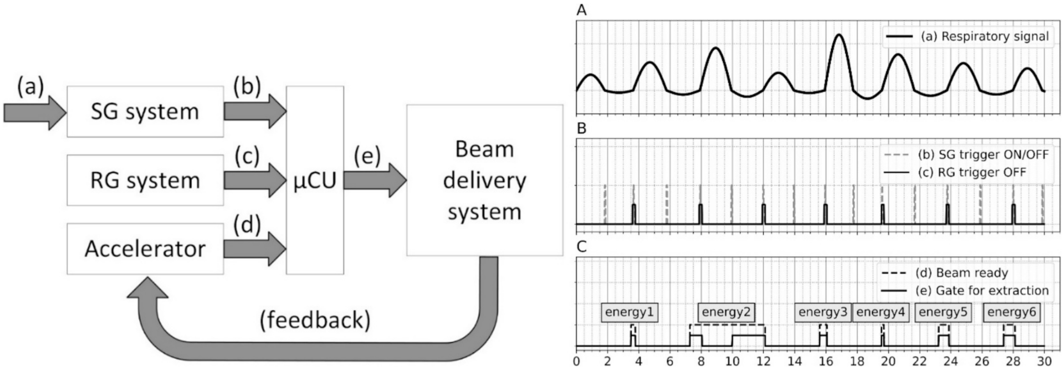

Fig. 9. Surface combined with range guided motion management conceptual schematic (left panel) and motion management main control signals (right panel): (A) a patient respiratory signal (a) obtained by surface guided sensor; (B) triggers provided by surface guided (b) and range guided (c) systems; (C) a signal (d) from accelerator that beam is accelerated and ready for extraction, and a resulting signal (e) allowed beam delivery.

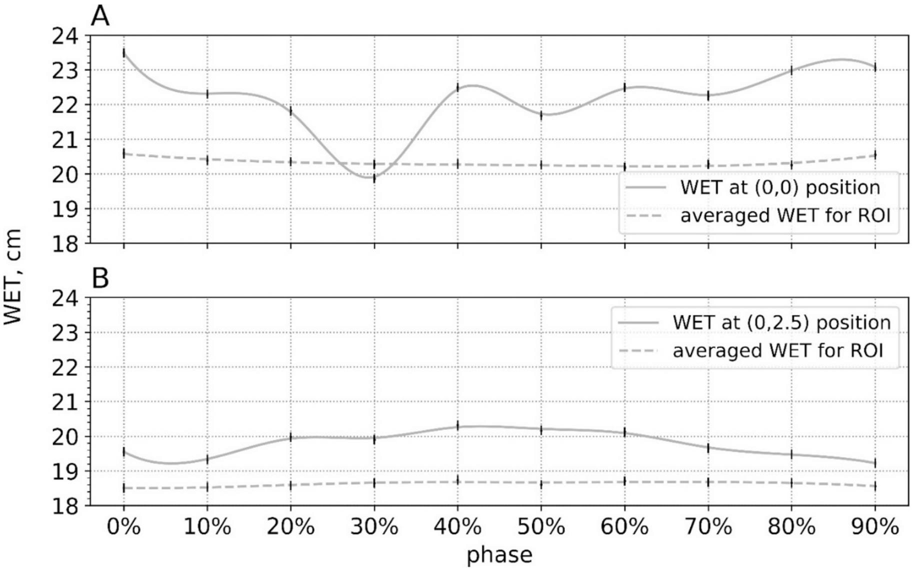

Fig. 10. WET values for every phase of 4DCT data were obtained from single energy layers, as shown in Fig. 7: (A) 1st field; (B) 2nd field.

implementation, given the data on the moving phantom presented in this paper. In fact, this experiment is an *iso*-energy layer analysis with a certain (sufficiently large for a real irradiated area) scan pattern. At the same time, the concept of single spot tracking is still an unsolved technical challenge, whose complexity lies in the small amount of data and its high noise. Future engineering work will focus on solving this problem. The next challenge will be the adaptive treatment, the creation of a universal range-adapted plan. In the framework of this work, we have only shown the plan adapted to one phase of 4DCT data and the absolute difference to other phases. In this direction, the focus of research will be on *iso*-energy layer-by-layer analysis and the formation of a universal plan based on this information.

Finally, we would like to address the limitations of the current study and outline ongoing steps for improvement. First, we are preparing experimental pRad and HeRad imaging using a more advanced moving respiratory phantom equipped with internal markers to quantify the differences between the two modalities and to compare images acquired in 4DCT under continuous motion. Second, the same phantoms will be irradiated with a pure carbon beam to evaluate the influence of fragments on the detector and to develop a method for separating fragment signals from the useful helium signal in mixed beam irradiation scenarios. Third, while the dynamic pRad and HeRad Monte Carlo simulation model has only been applied to simple geometries (such as the phantom used in this study), patient data has been analyzed under static assumptions. Future work will investigate continuously moving patient geometries to account for anatomical shifts between phase-binned data sets while considering beam scan time and scan patterns. Fourth, we plan to introduce irregularities in the initial data and attempt to reconstruct more complex motion patterns. Finally, the current experimental images suffer from noise, especially in dynamic mode, where the number of protons or helium ions available per image is limited. This will require further hardware improvements and the application of noise suppression algorithms.

5. Conclusions

This study investigated low-dose proton and helium radiography using pencil beam scanning for motion management in radiotherapy. For the first time, the technical feasibility of using particle radiography to track motion patterns with clinically required temporal resolution was demonstrated using small (10 cm × 10 cm) fields on a simple respiratory phantom with scanning proton and helium beams from two particle therapy centers.

It was shown that low-dose helium radiography modeled from 4DCT data can effectively detect intrafractional anatomical changes. Two strategies for using helium radiography for real-time monitoring of mixed carbon-helium beam therapy – single energy analysis and single spot range probing – were proposed and discussed, with the former showing promise in reconstructing motion-induced anatomical changes. Future work in this direction considers the performance of mixed carbon-helium beam experiments and the development of an intrafractional motion management system for single energy analysis for synchrotron-based particle therapy facilities.

Declaration of competing interest

The authors declare that they have no known competing financial interests or personal relationships that could have appeared to influence the work reported in this paper.

Acknowledgments

We would like to thank Edith Baader for organizing the data acquisition with 4DCT, Dr. Eike Feldmeier for providing accurate data on the particle beam from the HIT synchrotron, and Dr. Stephan Brons for his invaluable help with a beamtime at HIT.

The work was funded by the Deutsche Forschungsgemeinschaft (DFG, German Research Foundation) – Project No.\ 457509854.

References

[1] Grau C, Durante M, Georg D, Langendijk JA, Weber DC. Particle therapy in Europe. Mol Oncol 2020;14(7):1492–9. https://doi.org/10.1002/1878-0261.12677.

[2] Riboldi M, Orecchia R, Baroni G. Real-time tumour tracking in particle therapy: technological developments and future perspectives. Lancet Oncol 2012;13(9). https://doi.org/10.1016/S1470-2045(12)70243-7. e383–e391.

[3] Bert C, Durante M. Motion in radiotherapy: particle therapy. Phys Med Biol 2011; 56(16):R113. https://doi.org/10.1088/0031-9155/56/16/R01.

[4] He P, Mori S. Perturbation analysis of 4D dose distribution for scanned carbon-ion beam radiotherapy. Phys Med 2020;74:74–82. https://doi.org/10.1016/j.ejmp.2020.05.003.

[5] Lomax AJ. Intensity modulated proton therapy and its sensitivity to treatment uncertainties 1: the potential effects of calculational uncertainties. Phys Med Biol 2008;53(4):1027. https://doi.org/10.1088/0031-9155/53/4/014.

[6] Liao Z, Lee JJ, Komaki R, Gomez DR, O'Reilly MS, Fossella FV, et al. Bayesian adaptive randomization trial of passive scattering proton therapy and intensity-modulated photon radiotherapy for locally advanced non–small-cell lung cancer. Clin Oncol 2018;36(18):1813–22. https://doi.org/10.1200/JCO.2017.74.0720.

[7] Lomax AJ. Intensity modulated proton therapy and its sensitivity to treatment uncertainties 2: the potential effects of inter-fraction and inter-field motions. Phys Med Biol 2008;53(4):1043. https://doi.org/10.1088/0031-9155/53/4/015.

[8] Takao S, Miyamoto N, Matsuura T, Onimaru R, Katoh N, Inoue T, et al. Intrafractional baseline shift or drift of lung tumor motion during gated radiation therapy with a real-time tumor-tracking system. Int J Radiat Oncol Biol Phys 2016;94(1):172–80. https://doi.org/10.1016/j.ijrobp.2015.09.024.

[9] Dhont J, Vandemeulebroucke J, Burghelea M, Poels K, Depuydt T, Van Den Begin R, et al. The long- and short-term variability of breathing induced tumor motion in lung and liver over the course of a radiotherapy treatment. Radiother Oncol 2018;126(2):339–46. https://doi.org/10.1016/j.radonc.2017.09.001.

[10] Keall PJ, Mageras GS, Balter JM, Emery RS, Forster KM, Jiang SB, et al. The management of respiratory motion in radiation oncology report of AAPM Task Group 76a). Med Phys 2006;33:3874–900. https://doi.org/10.1118/1.2349696.

[11] Mastella, Molinelli E, Pella S, Vai A, Maestri A, Vitolo D, et al. 4D strategies for lung tumors treated with hypofractionated scanning proton beam therapy: dosimetric impact and robustness to interplay effects. Radiother Oncol 2020;146:213–20. https://doi.org/10.1016/j.radonc.2020.02.025.

[12] Rietzel E, Pan T, Chen GTY. Four-dimensional computed tomography: image formation and clinical protocol. Med Phys 2005;32:874–89. https://doi.org/10.1118/1.1869852.

[13] Pakela JM, Knopf A, Dong L, Rucinski A, Zou W. Management of motion and anatomical variations in charged particle therapy: past, present, and into the future. Front Oncol 2022;12. https://doi.org/10.3389/fonc.2022.806153.

[14] Chang JY, Zhang X, Knopf A, Li H, Mori S, Dong L, et al. Consensus guidelines for implementing pencil-beam scanning proton therapy for thoracic malignancies on behalf of the PTCOG thoracic and lymphoma subcommittee. Int J Radiat Oncol Biol Phys 2017;99(1):41–50. https://doi.org/10.1016/j.ijrobp.2017.05.014.

[15] Kang Y, Zhang X, Chang JY, Wang H, Wei X, Liao Z, et al. 4D Proton treatment planning strategy for mobile lung tumors. Int J Radiat Oncol Biol Phys 2007;67(3):906–14. https://doi.org/10.1016/j.ijrobp.2006.10.045.

[16] Seco J, Robertson D, Trofimov A, Paganetti H. Breathing interplay effects during proton beam scanning: simulation and statistical analysis. Phys Med Biol 2009;54(14):N283. https://doi.org/10.1088/0031-9155/54/14/N01.

[17] Ebner DK, Tsuji H, Yasuda S, Yamamoto N, Mori S, Kamada T. Respiration-gated fast-rescanning carbon-ion radiotherapy. Jpn J Clin Oncol 2017;47(1):80–3. https://doi.org/10.1093/jjco/hyw144.

[18] Graeff C, Constantinescu A, Lüchtenborg R, Durante M, Bert C. Multigating, a 4D optimized beam tracking in scanned ion beam therapy. Technol Cancer Res Treat 2014;13(6):497–504. https://doi.org/10.7785/tcrtexpress.2013.600277.

[19] Kanai T, Paz A, Furuichi W, Liu CS, He P, Mori S. Four-dimensional carbon-ion pencil beam treatment planning comparison between robust optimization and range-adapted internal target volume for respiratory-gated liver and lung treatment. Phys Med 2020;80:277–87. https://doi.org/10.1016/j.ejmp.2020.11.009.

[20] Schulte R, Bashkirov V, Li T, Liang Z, Mueller K, Heimann J, et al. Conceptual design of a proton computed tomography system for applications in proton radiation therapy. IEEE T Nucl Sci 2004;51(3):866–72. https://doi.org/10.1109/TNS.2004.829392.

[21] Graeff C, Weber U, Schuy C, Saito N, Volz L, Piersimoni P, et al. [OA027] Helium as a range probe in carbon ion therapy. Phys Med 2018;52:11. https://doi.org/10.1016/j.ejmp.2018.06.099.

[22] Mazzucconi D, Agosteo S, Ferrarini M, Fontana L, Lante V, Pullia M, et al. Mixed particle beam for simultaneous treatment and online range verification in carbon ion therapy: proof-of-concept study. Med Phys 2018;45:5234–43. https://doi.org/10.1002/mp.13219.

[23] Volz L, Kelleter L, Brons S, Burigo L, Graeff C, Niebuhr NI, et al. Experimental exploration of a mixed helium/carbon beam for online treatment monitoring in carbon ion beam therapy. Phys Med Biol 2020;65(5):055002. https://doi.org/10.1088/1361-6560/ab6e52.

[24] Devicienti S, Strigari L, D'Andrea M, Benassi M, Dimiccoli V, Portaluri M. Patient positioning in the proton radiotherapy era. J Exp Clin Cancer Res 2010;29(1):47. https://doi.org/10.1186/1756-9966-29-47.

[25] Hammi A, Koenig S, Weber DC, Poppe B, Lomax AJ. Patient positioning verification for proton therapy using proton radiography. Phys Med Biol 2018;63(24):245009. https://doi.org/10.1088/1361-6560/aadf79.

[26] Meijers A, Seller OC, Free J, Bondesson D, Oria CS, Rabe M, et al. Assessment of range uncertainty in lung-like tissue using a porcine lung phantom and proton radiography. Phys Med Biol 2020;65(15):155014. https://doi.org/10.1088/1361-6560/ab91db.

[27] DeJongh EA, DeJongh DF, Polnyi I, Rykalin V, Sarosiek C, Coutrakon G, et al. Technical Note: a fast and monolithic prototype clinical proton radiography system optimized for pencil beam scanning. Med Phys 2021;48:1356–64. https://doi.org/10.1002/mp.14700.

[28] DeJongh DF, DeJongh EA, Rykalin V, DeFillippo G, Pankuch M, Best AW, et al. A comparison of proton stopping power measured with proton CT and x-ray CT in fresh postmortem porcine structures. Med Phys 2021;48:7998–8009. https://doi.org/10.1002/mp.15334.

[29] Sarosiek C, DeJongh EA, Coutrakon G, DeJongh DF, Duffin KL, Karonis NT, et al. Analysis of characteristics of images acquired with a prototype clinical proton radiography system. Med Phys 2021;48:2271–8. https://doi.org/10.1002/mp.14801.

[30] DeJongh DF, DeJongh EA. An iterative least squares method for proton CT image reconstruction. IEEE T Radiat Plasma Med Sci 2022;6(3):304–12. https://doi.org/10.1109/trpms.2021.3079140.

[31] Kleffner C, Ondreka D, Weinrich U. The Heidelberg Ion Therapy (HIT) accelerator coming into operation. AIP Conference Proceedings 2009;1099(1):426–8. https://doi.org/10.1063/1.3120065.

[32] Parodi K, Mairani A, Brons S, Hasch BG, Sommerer F, Naumann J, et al. Monte Carlo simulations to support start-up and treatment planning of scanned proton and carbon ion therapy at a synchrotron-based facility. Phys Med Biol 2012;57(12):3759. https://doi.org/10.1088/0031-9155/57/12/3759.

[33] Perl J, Shin J, Schümann J, Faddegon B, Paganetti H. TOPAS: An innovative proton Monte Carlo platform for research and clinical applications. Med Phys 2012;39:6818–37. https://doi.org/10.1118/1.4758060.

[34] Faddegon B, Ramos-Méndez J, Schuemann J, McNamara A, Shin J, Perl J, et al. The TOPAS tool for particle simulation, a Monte Carlo simulation tool for physics, biology and clinical research. Phys Med 2020;72:114–21. https://doi.org/10.1016/j.ejmp.2020.03.019.

[35] Dedes G, Dickmann J, Giacometti V, Rit S, Krah N, Meyer S, et al. The role of Monte Carlo simulation in understanding the performance of proton computed tomography. Z Med Phys 2022;32(1):23–38. https://doi.org/10.1016/j.zemedi.2020.06.00.

[36] Tripathi RK, Cucinotta FA, Wilson JW. Accurate universal parameterization of absorption cross sections III – light systems. Nucl Instrum Methods Phys Res B 1999;155(4):349–56. https://doi.org/10.1016/S0168-583X(99)00479-6.

[37] Horst F, Aricò G, Brinkmann KT, Brons S, Ferrari A, Haberer T, et al. Measurement of 4He charge- and mass-changing cross sections on H, C, O, and Si targets in the energy range 70–220 MeV/u for radiation transport calculations in ion-beam therapy. PhysRevC9 2019;99:014603. https://doi.org/10.1103/PhysRevC.99.014603.

[38] Schneider W, Bortfeld T, Schlegel W. Correlation between CT numbers and tissue parameters needed for Monte Carlo simulations of clinical dose distributions. Phys Med Biol 2000;45(2):459. https://doi.org/10.1088/0031-9155/45/2/314.

[39] Hugo GD, Weiss E, Sleeman WC, Balik S, Keall PJ, Lu J, et al. A longitudinal four-dimensional computed tomography and cone beam computed tomography dataset for image-guided radiation therapy research in lung cancer. Med Phys 2017;44:762–71. https://doi.org/10.1002/mp.12059.

[40] Hardt JJ, Pryanichnikov AA, Homolka N, DeJongh EA, DeJongh DF, Cristoforetti R, et al. The potential of mixed carbon-helium beams for online treatment verification: a simulation and treatment planning study. Phys Med Biol 2024;69(12). https://doi.org/10.1088/1361-6560/ad46db.

[41] Wieser H-P, Cisternas E, Wahl N, Ulrich S, Stadler A, Mescher H, et al. Development of the open-source dose calculation and optimization toolkit matRad. Med Phys 2017;44:2556–68. https://doi.org/10.1002/mp.12251.

[42] Ackermann B, Bangert M, Bennan ABA, Burigo L, Cabal G, Cisternas E, et al. e0404/matRad: Blaise v2.10.1 (2.10.1). Zenodo 2020. https://doi.org/10.5281/zenodo.7107719.

[43] Belikhin M, Pryanichnikov A, Balakin V, Shemyakov A, Zhogolev P, Chernyaev A. High-speed low-noise optical respiratory monitoring for spot scanning proton therapy. Phys Med 2023;112:102612. https://doi.org/10.1016/j.ejmp.2023.102612.

[44] DeJongh EA, Pryanichnikov AA, DeJongh DF, Schulte RW. A stopping criterion for iterative proton CT image reconstruction based on correlated noise properties. J Appl Clin Med Phys 2023;24:e14114. https://doi.org/10.1002/acm2.14114.

[45] Kügele M, Mannerberg A, Nørring Bekke S, Alkner S, Berg L, Mahmood F, et al. Surface guided radiotherapy (SGRT) improves breast cancer patient setup accuracy. J Appl Clin Med Phys 2019;20:61–8. https://doi.org/10.1002/acm2.12700.